Acta Materialia 181 (2019) 510–518

Contents lists available at ScienceDirect

Acta Materialia

journal homepage: www.elsevier.com/locate/actamat

Full length article

Unsupervised learning of dislocation motion

Darren C. Pagan[a,*], Thien Q. Phan[b], Jordan S. Weaver[b], Austin R. Benson[c], Armand J. Beaudoin[a,d]

[a] Cornell High Energy Synchrotron Source, Cornell University, Ithaca, NY 14853, USA
[b] Engineering Laboratory, National Institute of Standards and Technology, Gaithersburg, MD 20899, USA
[c] Department of Computer Science, Cornell University, Ithaca, NY 14853, USA
[d] Department of Mechanical Science and Engineering, University of Illinois at Urbana-Champaign, Urbana, IL 61801, USA

ARTICLE INFO

Article history:
Received 8 July 2019
Revised 4 October 2019
Accepted 9 October 2019
Available online 14 October 2019

Keywords:
Plasticity
Machine learning
Additive manufacturing
X-ray diffraction
Nickel-based superalloy

ABSTRACT

The unsupervised learning technique, locally linear embedding (LLE), is applied to the analysis of X-ray diffraction data measured *in-situ* during the uniaxial plastic deformation of an additively manufactured nickel-based superalloy. With the aid of a physics-based material model, we find that the lower-dimensional coordinates determined using LLE appear to be physically significant and reflect the evolution of the defect densities that dictate strength and plastic flow behavior in the alloy. The implications of the findings for future constitutive model development are discussed, with a focus on wider applicability to microstructure evolution and phase transformation studies during *in-situ* materials processing.

1. Introduction

The study of plasticity in engineering alloys is primarily a study of dislocation motion. Material scientists forensically observe the configurations of dislocations before and after deformation, then attempt to correlate these configurations to mechanical response, while mechanicians attempt to model mechanical response during plasticity with implicit representations of underlying dislocation configurations (state variables). The challenge of this research is distilling something as complex as the evolution of tangled dislocation structures down to a system of differential equations that can be used to predict mechanical response. In this paper, we demonstrate that unsupervised learning techniques which reduce the dimensionality of data are capable of addressing this long-standing challenge at the heart of modeling plasticity in engineering alloys. Specifically, the reconfiguration of atoms and defects expressed in diffraction data serve as 'articulation points' [1] to be found with unsupervised learning. In addition, with these reduced dimensionality representations of microstructure, the modeling of plasticity behavior can shift from the sole fitting of state variables using mechanical response data to a more direct alignment of lower-dimensional embeddings that characterize the microstructure with solutions to differential equations for evolution.

The past twenty years have seen vast strides forward in developing diffraction-based characterization techniques, electron-, X-ray-, and neutron-based, that probe engineering alloys during *in-situ* processing and thermo-mechanical loading at increasingly short time scales. However, the full utility of these experiments is limited in that the analyses of the measured data extract only a fraction of the encoded information about the microstructure at any given time. As such, analysis tasks that appear to be relatively straight-forward at first impression, such as objectively identifying when subtle microstructural evolution or phase transformation begins to occur, can be difficult to perform. A researcher must know in advance to consider a structural feature in the data analysis model, limiting avenues of discovery of unexpected physical processes. For the case of diffraction peak analysis, different peak features can be used to extract various microstructural information: the centroid position of a diffraction peak is related to the spatial location, average elastic strain state, and average orientation of the grain from which it was emitted [2,3], while the shape of the diffraction peak is related to the size [4], morphology [5,6], and defect content (point, line, and planar defects) [7] of the grain. Though these quantities currently cannot be isolated and extracted from a single diffraction peak measured from a grain, their presence is encoded into the data. So as the microstructural configuration of grains within a specimen begin to evolve due to plastic deformation and motion of defects, so do the diffraction peaks.

This problem of extracting targeted microstructural information from a diffraction image falls under a broad data-science challenge

* Corresponding author.
E-mail address: dcp99@cornell.edu (D.C. Pagan).

https://doi.org/10.1016/j.actamat.2019.10.011
1359-6454/

known as dimensionality reduction. The goal of the process is to distill a high-dimensional measurement, like a diffraction image, down to a few values that are more readily analyzed. Concurrent with advances in microstructural characterization techniques, an array of unsupervised learning techniques has been developed for performing this dimensionality reduction on data that do not lie on linear planes in high-dimensional space (non-linear manifolds) [8]. These advances are of particular interest for performing dimensionality reduction on microstructural data (both in real and reciprocal space), as the evolution of microstructure due to thermo-mechanical loading is also highly non-linear, so it is expected that the data lie on non-linear manifolds. Applying these data-analysis approaches to microstructural data can provide the benefit of far fewer *a-priori* assumptions that must be made regarding the data prior to analysis in comparison to traditional physics-based inversion methods, allowing for novel discoveries regarding material understanding to be more readily made.

Rather than analyze diffraction data with a physics-based X-ray model to try to extract structural information chosen *a priori*, we propose the use of the unsupervised learning technique, locally linear embedding (LLE), to condense X-ray data down to critical microstructural (dislocation configuration) evolution information. The LLE method finds a set of coordinates in a lower-dimensional space that maintains the local neighborhood character (similarity or dissimilarity) of nearby data observations [9]. While LLE will determine similarity in a tractable representation, physical understanding still comes from discovering what underlying features or physical processes maintains the neighborhood character. We apply LLE directly to *in-situ* X-ray diffraction data to discover and monitor underlying dislocation motion in an additively manufactured (AM) nickel-based superalloy, Inconel 625 (IN625). We find that in this case, the LLE analysis of time series X-ray diffraction data identifies, without intervention, both the onset of plastic deformation (yield) and transients associated with the mobility of dislocation populations that underlie the strength and plasticity behavior in the alloy. We emphasize however that this is a single demonstration and the approach can be applied to numerous other studies of deformation and materials processing.

The structure of the paper is as follows. The material tested will be described in Section 2, while the experimental and data processing methods are given in Section 3. The material model used interpret the lower-dimensional representation of the microstructure is summarized in Section 4. The lower dimensional embeddings from the diffraction data are presented and compared to state evolution from the material model in Section 5. The results are then further discussed in Section 6 with a focus on applicability of this analysis to other loading conditions.

2. Material

The additively manufactured Inconel 625 (AM IN625) specimen was produced at the National Institute of Standards and Technology (NIST) using laser powder bed fusion in an EOS INT M290 system[1] following the manufacturer's nominal build recommendations. The laser power and velocity were 285 W and 960 mm/s, respectively, with 40 µm thick build layers. The hatch distance between scan tracks was 110 µm. The powder feedstock was supplied by the manufacturer and the chemical composition is similar to those reported in other works [10]. An AM block measuring 25.4 mm × 25.4 mm × 32 mm (width × length × height) was deposited directly onto the build plate. The block and build plate were stress-relieved (SR) heat treated at 800 °C for 1 h to reduce the formation of deleterious phases [10]. The block was then removed via wire electro-discharge machining (EDM) and post-processed via hot isostatic pressing (HIP) at 1175 °C and 152 MPa for 4 h in an argon atmosphere according to ASTM F3056 [11]. Uniaxial tension test specimens were machined from the HIP-ed block using wire EDM such that the build direction is parallel to the tensile direction.

A 10 mm × 10 mm × 20 mm (width × length × height) sample in the SR+HIP condition was cross-sectioned and polished for electron backscatter diffraction (EBSD) grain morphology and orientation characterization. A final vibratory polish was made with 0.02 µm colloidal silica. EBSD measurements were performed with a JOEL JSM7100 field-emission scanning electron microscope (SEM) with Oxford EBSD detector[1]. A step size of 1.5 µm was used for scans covering an area approximately 1 mm × 0.5 mm. EBSD analysis was done in MTEX [12]. The measured orientation fields from different planes of the AM IN625 material are shown in Fig. 1a and Fig. 1b. Fig. 1a shows a plane perpendicular to the build direction (Z-Plane [13]) and Fig. 1b shows a plane with its normal direction perpendicular to the build and recoating directions (Y-Plane [13]). The orientation fields are colored by the direction of surface normal on the inverse pole figure maps with the grain boundaries drawn in black. From the figure, we can see the heat treatment has generally removed microstructure anisotropy of both grain morphology and preferred orientation between the build and transverse directions. Grains were identified using a minimum misorientation angle of 5° and minimum size greater than 9 pixels (equivalent circular area radius of 2.5 µm). The cross sections of the microstructure are similar between the two planes indicating a fairly equiaxed microstructure with an average grain size of 22.6 µm ± 7.3 µm and 20.6 µm ± 6.9 µm for the Z and Y planes, respectively. This grain size can be compared to wrought (rolled then annealed at 870 °C for 1 h in vacuum) IN625 plate with a grain size of 5.1 µm ± 1.7 µm. The microstructure was also found to contain a significant quantity of grain boundaries associated with twin related domains ($\Sigma 3$ grain boundaries). The measured line fraction of $\Sigma 3$ boundaries was 0.69 ± 0.03 for the Z-Plane and 0.68 ± 0.03 for Y-Plane, which can be compared to 0.55 ± 0.3 in wrought plate.

3. Methods

3.1. Experiment

A time series, 38 loading points (observations), of evolving X-ray diffraction peaks was measured in a transmission geometry as the AM IN625 specimen was deformed in uniaxial tension to a macroscopic strain (ε) of 0.03 (3%). A schematic of the experimental geometry is given in Fig. 3. The IN625 specimen was loaded along the AM build direction. The cross section of the specimen was 1 mm × 1 mm and the full sample gauge length was 8 mm. The specimen was deformed in uniaxial tension in the RAMS2 load frame [14] at sector ID1-A3 of the Cornell High Energy Synchrotron Source (CHESS). The specimen was deformed in displacement control at a rate of 10 nm/s along the $\boldsymbol{y}$ direction. The macroscopic stress (σ) and strain points (marked with red x's) at which diffraction measurements were made are shown in Fig. 2a.

The full cross section of the AM IN625 specimen was illuminated by a 61.332 keV (wavelength of 0.0202 nm) X-ray beam. The X-ray beam, which was 1 mm tall by 2 mm wide, illuminated a volume at the center of the gauge section and traveled in the $-\boldsymbol{z}$ direction. As the sample was deformed, the sample was also continuously rotated (rocked) about the $\boldsymbol{y}$ direction to rotate more crystals into the diffraction condition. Diffraction peaks from a 10° rocking motion were integrated onto single images for processing. The measurement points of diffracted intensity as the sample was deformed are marked in Fig. 2a. The diffraction data was collected on

[1] Mention of commercial products does not imply endorsement by the National Institute of Standards and Technology, nor does it imply that such products or services are necessarily the best available for the purpose.

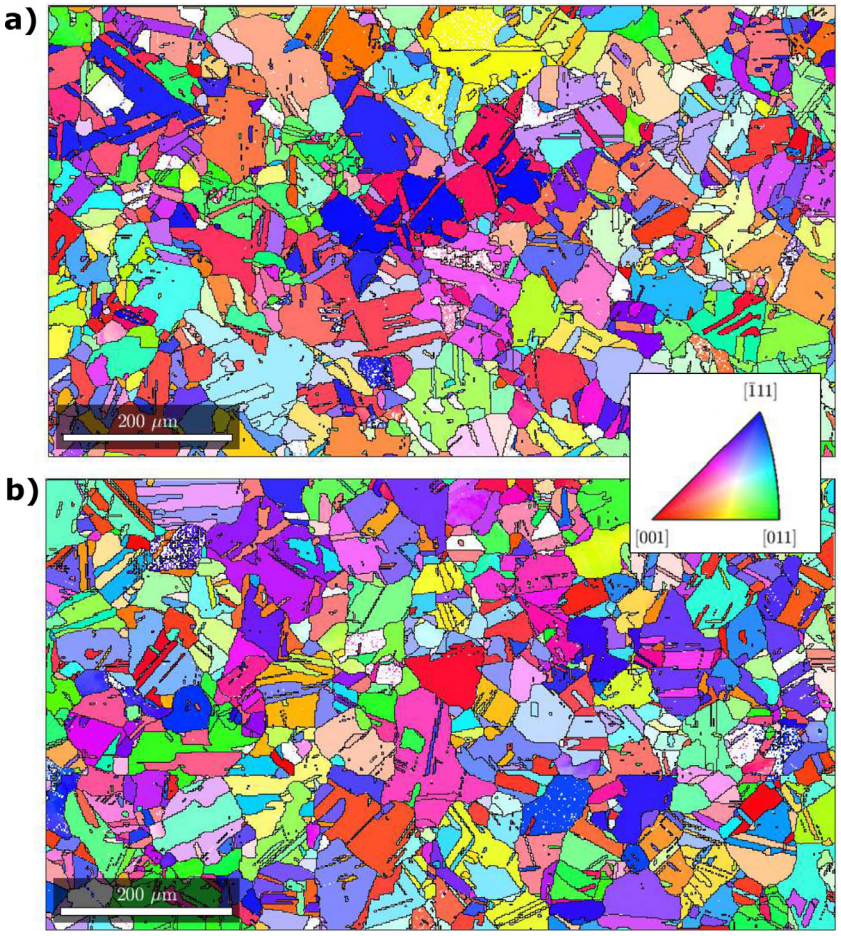

Fig. 1. (a) Crystal lattice orientation field perpendicular to the build direction in the AM IN625 (Z-Plane [13]). (b) Crystal lattice orientation field in the plane defined by the build direction and recoating direction in the AM IN625 (Y-Plane [13]). Coloring corresponds to the orientation of the surface normal in the crystal coordinate system on the inverse pole figure.

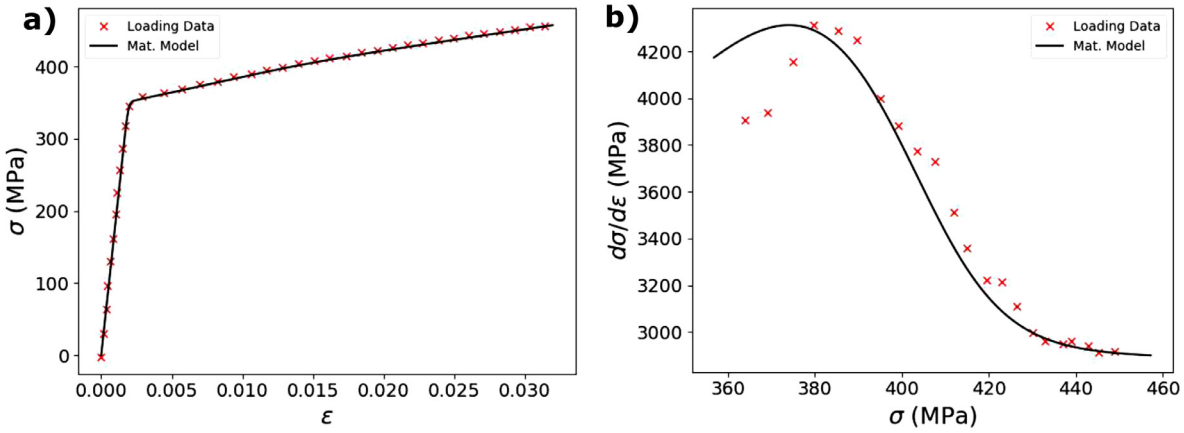

Fig. 2. (a) The macroscopic stress–strain response for the AM IN625 specimen tested in this work. (b) Material hardening rate ($d\sigma/d\varepsilon$) after the IN625 had begun to yield. Points at which diffraction measurements were made are indicated with red x's. The material response from the fit material model is shown with solid lines.

a Dexela 2923 area detector sitting 877 mm behind the specimen every 470 s. The detector was translated horizontally 135 mm from the direct X-ray beam to prevent collection of diffraction peaks near the rotation axis that would provide misleading characterization of the microstructure evolution.

3.2. Data analysis

An example diffraction image measured prior to loading is shown in Fig. 4a. As can be seen, the measured diffraction peaks lie on tight rings (full rings are only partially captured in the experimental geometry used), with each ring corresponding to families of crystallographic lattice planes with varied spacing, leaving most of the detector empty. Prior to LLE analysis, 75° arcs of diffraction peaks from the first four rings / families of lattice planes ({111}, {200}, {220}, and {311}) were extracted, remapped to a polar coordinate system, and then concatenated into a single image for each load point. The arc length chosen nearly spans over the X-ray detector as-positioned. This process and examples are shown in Fig. 4b. Fig. 4b shows the first few and final sets of diffraction

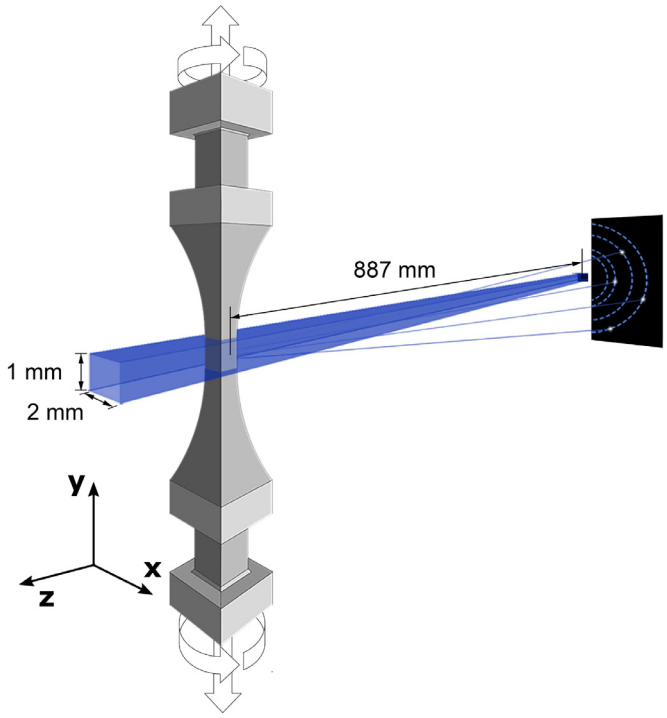

Fig. 3. Schematic of the experimental configuration for the *in-situ* X-ray measurements made during the uniaxial loading of the AM IN625 specimen.

peaks from the IN625 specimen. Clear evolution from sharp peaks to a 'smeared' diffracted signal as strain is applied can be observed. Again, this peak evolution is directly related to internal structure changes. Lastly before LLE analysis, the diffraction peaks from each measurement are transformed into column vectors $\boldsymbol{X}$ of a data matrix. In total, the data matrix size is 38 observations by 7.5 million features, as each pixel of the reduced peak data is treated as an independent feature.

The data matrix is analyzed using the LLE algorithm [9,15] available in Scikit-Learn [16]. First, scalar weights w that reconstruct an observation $\boldsymbol{X}$ from its nearest neighbors are determined, with a neighbor being an observation that is close in distance. The weights are found by minimizing the error e between an observation and its reconstruction from a chosen number of neighbors (weights of non-neighbors are set to 0)

$$e = \sum_i \left| \boldsymbol{X_i} - w_{ij} \boldsymbol{X_j} \right|^2 \tag{1}$$

and constraining the sum of the non-zero weights for each reconstruction to be equal to 1. This linear combination of neighboring observations makes up the 'locally linear' portion of LLE. An example matrix of weights found from the 38 points using 5 neighbors is shown in Fig. 5. In this special case, the diffraction peaks from a load step are reconstructed from weighed contributions of neighbors that also happen to be adjacent points in time. This can be seen in Fig. 5 as the observations are ordered by time / applied strain and all weights are clustered around the diagonal of the matrix. A cost function ϕ is then minimized to find sets of embedded coordinates (or simply an embedding) $\boldsymbol{Y}$ that approximately maintains the same normalized distance between neighboring observations by fixing the previously determined weights

$$\phi = \sum_i \left| \boldsymbol{Y_i} - w_{ij} \boldsymbol{Y_j} \right|^2. \tag{2}$$

The embedded coordinates $\boldsymbol{Y}$ are solved for by reorganizing the cost function into an eigenvalue problem, and the coordinates which best maintain the previously determined weights are those with the lowest eigenvalues.

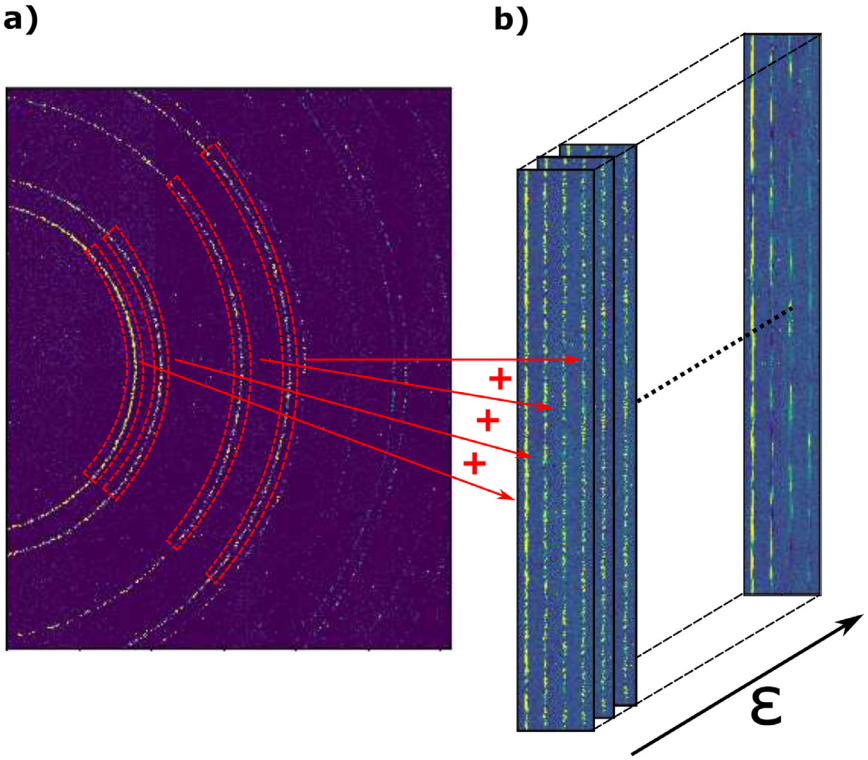

Fig. 4. (a) An example raw diffraction image collected from the deforming AM IN625 during uniaxial deformation. (b) Extracted diffraction peak data from the first four diffraction rings are collected and remapped into a polar coordinate system. The diffraction peaks evolve from the AM IN625 specimen with increasing macroscopic strain ε.

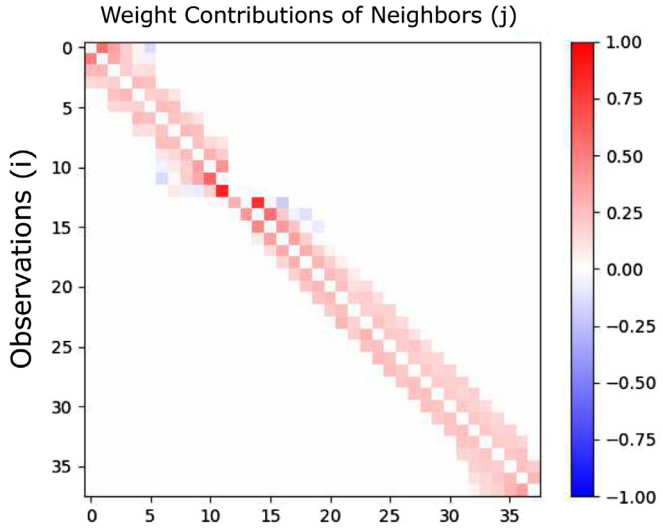

Fig. 5. Weights w calculated using Eq. (1). Each row corresponds to the weights used to reconstruct the embedding $\boldsymbol{Y}$.

Table 1
Elasticity moduli [20] used to fit the material deformation model.

E (GPa)	G (GPa)
182.0	71.2

4. Defect evolution model

The lower-dimensional microstructure data extracted using LLE will be interpreted through a well-established model developed by Estrin and Kubin [17], complemented by an additive decomposition of elastic and plastic strain rates and a simple power law relationship for rate dependence [18,19]. In the model, the plasticity behavior is dictated by two state variables, a mobile dislocation density ρ_m that influences the plastic strain rate at a fixed stress and an obstacle density ρ_f that controls the current yield strength of the alloy. Each of these state variables evolves as a function of plastic deformation. The growth of the mobile dislocation density ρ_m is modeled as a release from pinned positions, while the reduction of density is modeled as a repinning of dislocations that contribute to the obstacle density. Growth of the obstacle density ρ_f has a contribution from the mobile dislocation population and defect multiplication with plastic deformation.

In the model, the total strain rate is additively decomposed into elastic $\dot{\varepsilon}_E$ and plastic $\dot{\varepsilon}_P$ portions

$$\dot{\varepsilon} = \dot{\varepsilon}_E + \dot{\varepsilon}_P \tag{3}$$

and the rate of change of stress $\dot{\sigma}$ is linearly related to the elastic strain rate

$$\dot{\sigma} = E\dot{\varepsilon}_E \tag{4}$$

where E is Young's modulus. The plastic strain rate is related to the applied stress with a power law relationship

$$\dot{\varepsilon}_P = \rho_m b v_0 \left(\frac{\sigma}{\sigma_Y}\right)^{\frac{1}{m}} \tag{5}$$

where b is the Burgers vector, v_0 is the dislocation ensemble velocity, σ_Y is the yield strength, and m is the strain rate sensitivity. The yield strength in Eq. (5) is related to the obstacle density as

$$\sigma_y = M\alpha G b\sqrt{\rho_f} \tag{6}$$

where M is the Taylor factor, α is a proportionality constant, and G is the elastic shear modulus.

Both the mobile dislocation density and the obstacle density evolve with time and plastic deformation. The form of the evolution equations was proposed in [17] and in these evolution equations, the mobile and obstacle densities are coupled and evolve together in time. In our current formulation, terms related to dynamic recovery [19] are neglected as the sample was not sufficiently deformed to characterize these terms. The mobile density evolution in this formulation is given by

$$\dot{\rho_m} = \left(\frac{C_1}{b^2}(\rho_f/\rho_m) - \frac{C_2}{b}\sqrt{\rho_f}\right)\dot{\varepsilon}_P \tag{7}$$

while the obstacle density is given by

$$\dot{\rho_f} = \left(\frac{C_2}{b}\sqrt{\rho_f}\right)\dot{\varepsilon}_P. \tag{8}$$

For model evaluation, the specimen was deformed at a constant macroscopic strain rate $\dot{\varepsilon}$ of 2.25×10^{-6}, comparable to the experimental loading rate. The coupled set of differential equations are numerically integrated. The elastic moduli [20] can be found in Table 1, while the plasticity parameters can be found in Table 2. The plasticity material parameters used for the material model were chosen to capture the hardening response ($d\sigma/d\varepsilon$) of the alloy after yield. Fig. 2b shows the measured hardening response with red x's (derivative calculation facilitated by total variation regularization [21,22]) and the fit hardening response with a black line. The fit stress-strain response is also shown in Fig. 2a. In both figures, we see the major features of both the hardening rate and stress-strain response are captured with the model.

5. Results and analysis

5.1. Identifying onset of dislocation motion

The first three sets of embedded coordinates describing the measured diffraction peaks, as the number of neighbors used for reconstruction is increased, are shown in Figs. 6a–c. In these figures, LLE has reduced the 7.5 million features of each diffraction peak set down to three coordinates. The embedded coordinates are plotted versus the applied macroscopic strain at measurement since this quantity is a natural 'index' for the data. We note that each embedded coordinate is unique up to a sign (i.e., the sign of all values of the first embedded coordinate, Y_1, can be reversed), but in all figures, signs are chosen to facilitate interpretation and comparison to modeling of the evolution of defect densities. For all embedded coordinates in Fig. 7, the coordinates change relatively continuously with strain, as would be expected from microstructural evolution during uninterrupted loading.

The embedded coordinate that is most readily interpreted is embedded coordinate 1 (Fig. 7a). The coordinate initially is relatively constant until a macroscopic strain of 0.003, then begins to rapidly evolve until a saturation value is reached near the end of the test. Returning to Fig. 2, we find that the macroscopic strain of 0.003 corresponds to the relatively abrupt elastic-plastic transition

Table 2
Plasticity parameters used to the fit the material deformation model.

M	α	b (nm)	v_0 (m/s)	m	C_1	C_2	ρ_{m0} (1/m^2)	ρ_{f0} (1/m^2)
3	1/3	0.359	10^{-5}	20	8.0×10^{-5}	0.155	2.02×10^{14}	1.30×10^{15}

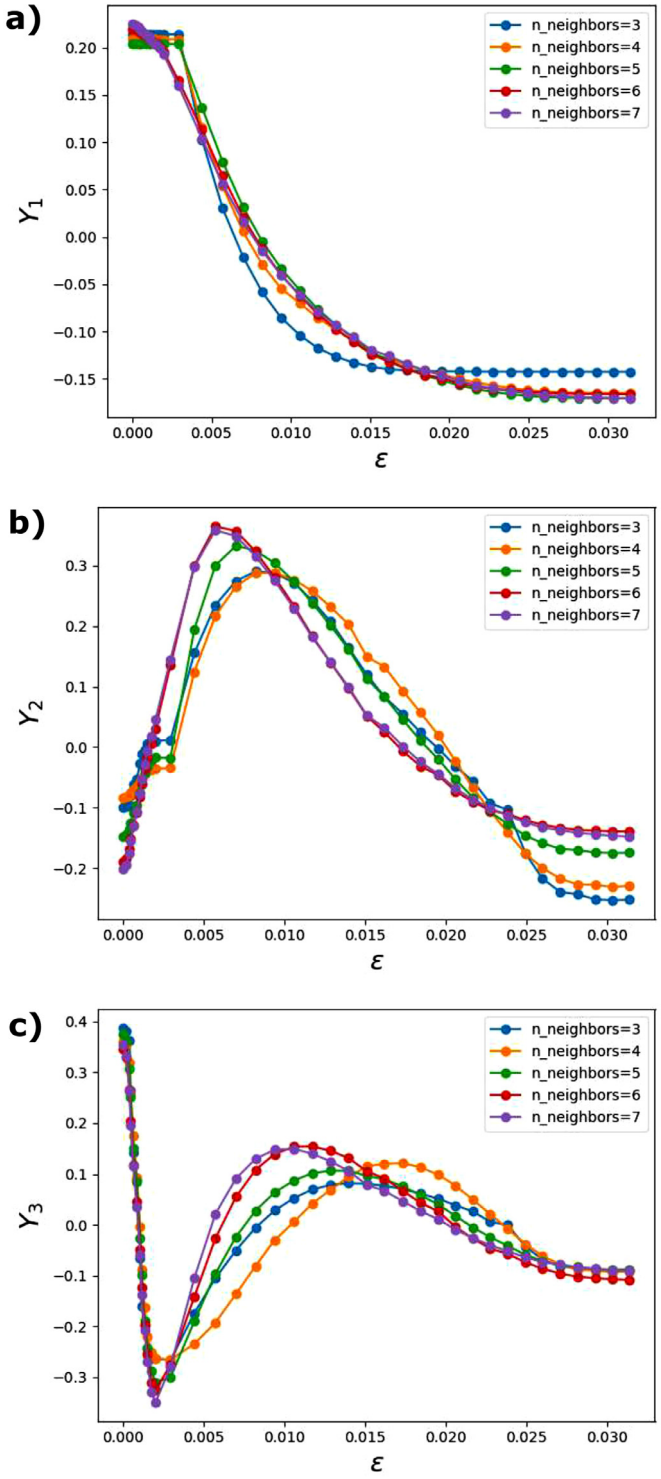

Fig. 6. Embedded coordinates plotted against macroscopic strain ε with increasing numbers of neighbors included for reconstruction. The first (a), second (b), and third (c) embedded coordinates are shown.

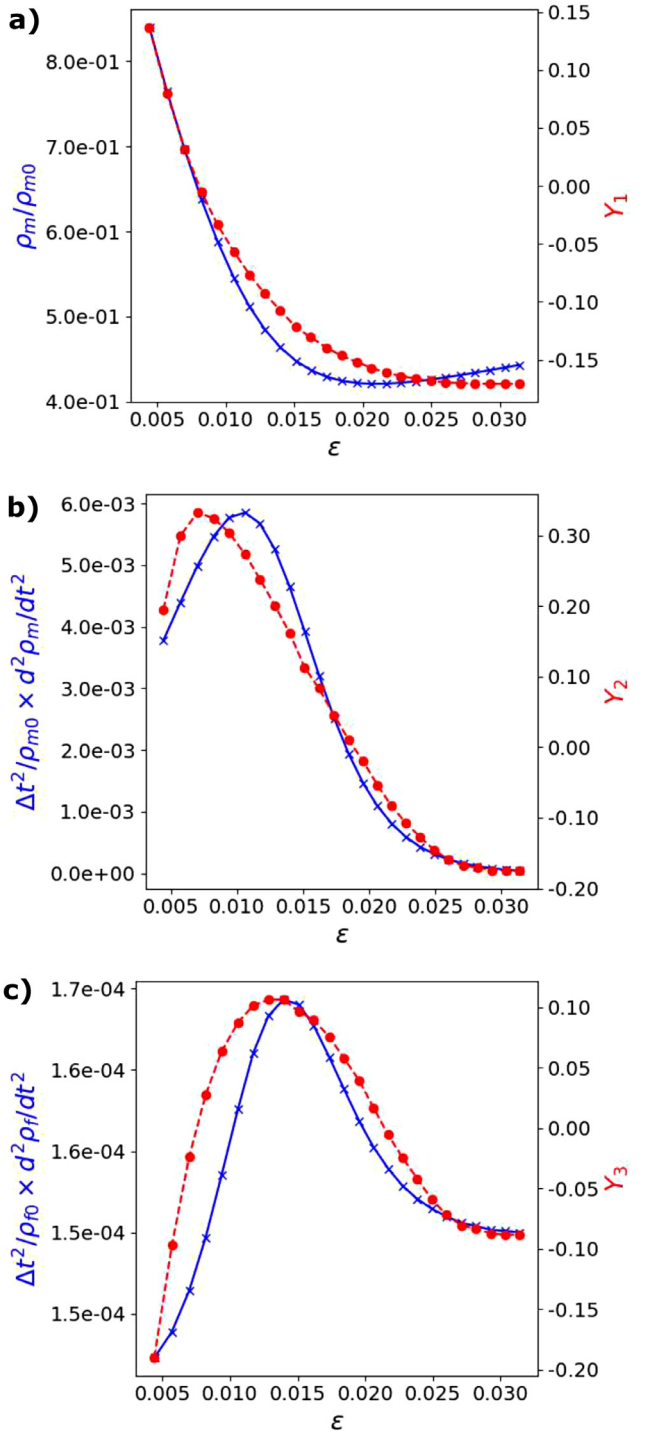

Fig. 7. (a) The evolution behavior of the model mobile dislocation density overlaid the first embedded coordinate. (b) The second derivative of the normalized model mobile dislocation density with respect to strain $d^2\rho_m/dt^2$ overlaid the second embedded coordinate Y_2. (c) The second derivative of the normalized model obstacle density with respect to strain $d^2\rho_f/dt^2$ overlaid the third embedded coordinate Y_3. Note that model quantities have been normalized by their initial densities and the time spacing between measurements Δt^2. We highlight that the LLE analysis only used diffraction peak intensities, while the material model was fit only to the macroscopic response. The LLE embedded coordinates were not trained to the model.

(yield point) of the AM IN625, indicating that embedded coordinate 1 is tied to the activation of a plastic deformation mechanism. As more neighbors are introduced, sharp behavioral transitions (like yield) begin to be 'averaged out' from the embeddings. In Fig. 7a, five is the largest number of neighbors used in observation reconstruction that still maintains the sharp behavior transition at macroscopic strain of 0.003. As such, all other analyses of embedded coordinates will use five neighbors and focus will be placed on embedded coordinates after yield ($\varepsilon > 0.003$). It is important to emphasize that in this analysis, the choice of neighbor count is driven by a physical understanding of the deformation process, not a computational limit.

As mentioned, simply determining when critical material evolution events are occurring objectively can be difficult. Here, direct unsupervised learning is locating a critical material evolution event and pinpointing the elastic-plastic transition in the deforming sample. Historically, the identification of the onset of yield is performed with a wide range of methods including manual identification of the transition to non-linearity in the macroscopic stress–strain response to semi-quantitative methods such as use of 0.2% strain offsets. The identification of the beginning of fully developed plasticity is even more challenging, with these methods typically revolving around analysis of stress or plastic strain rate evolution, both quantities being several steps removed from the underlying microstructure evolution associated with plastic deformation. In contrast, analysis of the first embedded coordinate of the diffraction peak time series is providing a straightforward solution to these issues. In Fig. 7a, we see that the beginning of the first embedded coordinate increase (or decrease depending on sign choice) neatly coincides with the elastic-plastic transition at $\varepsilon = 0.003$ and a corresponding yield stress of 358 MPa. Similarly, the first embedded coordinate appears to saturate at $\varepsilon = 0.026$ (although with not as clear of a distinction as the onset of yield), indicating the saturation of dislocation mobility and onset of steady state plastic flow.

5.2. Correlating dislocation mobility to embedded coordinates

To begin linking the lower-dimensional embedded coordinates and material state, the embedded coordinates after yielding are compared to the state variable evolution from the material model, as the state variables should link to articulation points of the microstructure and diffraction peak evolution. First, we find a strong correlation between the mobile dislocation density ρ_m and the first embedded coordinate (Y_1). The two quantities are overlaid in Fig. 7d. We also find significant similarities between the second derivative with respect to time of both the mobile dislocation and obstacle densities ($d^2\rho_m/dt^2$ and $d^2\rho_f/dt^2$) and the second and third embedded coordinates (Y_2 and Y_3). Fig. 7e and7f present the state variable second derivatives overlaid the embedded coordinates. The connection between the embedded coordinates and second derivatives of state will be described shortly. The similarities of inflection points between the state variable evolution and embedded coordinates with applied strain are striking. Most importantly, the similarities of relative distances in the embedded coordinates and the dislocation evolution in the model indicate that the lower-dimensional representation of the microstructure from LLE is linked to the dislocation mobility and the evolving defect densities in the alloy. *The LLE analysis used only the diffraction peak intensities while the material model was fit only to macroscopic mechanical response.* The LLE embedded coordinates were not trained to the model.

Drawing correspondence between the embedded coordinates and a material model is achieved by identifying evolution of defect populations as articulation points for observed diffraction peak evolution. We find that in this AM IN625, both the embedding and material model indicate that the primary driver of microstructure evolution is release, followed by rapid decrease, of mobile dislocation density at yield (Fig. 7d), of which roughly half are arrested within applied strain of 0.02. This is in contrast to the growth of a mobile dislocation density at yield in the model as originally proposed [17]. There are several possibilities for the initial large source of the mobile dislocation density in this material. First, the significant presence of annealing twins (see Section 2) may provide sources [23,24]. In addition, an initial release of dislocations from pinning solute may also be at work. Strain-aging effects are often observed in nickel superalloys [25], and aging effects have been shown to be present in heat-treated AM IN625 samples [26]. The arrest of mobile density due to dislocation solute interactions has been explored with a model for dynamic strain aging [27].

In some respects, the connection of the LLE embedded coordinates to state variables and their second derivatives is not completely unexpected. LLE belongs to a broader class of algorithms that, in effect, apply Laplacian operators (locally or globally) to the data of interest [1]. As part of this process, specifically observation-reconstruction in the LLE algorithm, a second differencing operation is performed and the eigenvector decomposition finds 'modes' of these operators. The takeaway from this insight is that beyond the state variables themselves, their second derivatives will also likely be correlated with embedded coordinates. This should be used as a guide for linking LLE embedded coordinates to physical processes in other material systems and thermo-mechanical loading conditions.

6. Discussion

The application of various machine learning techniques to materials science has promised to revolutionize the field, but to date, application to structural materials performance or processing has been limited. We foresee the approach demonstrated being applied to many other data types and material evolution conditions beyond X-ray diffraction data and uniaxial loading. Any time series of scattering data (electrons, neutrons, or X-rays) encoded with microstructural information will likely yield valuable insight, and the approach can also be applied to data gathered during other thermo-mechanical loading conditions and processing environments, specifically aiding Integrated Computational Materials Engineering (ICME) efforts [28]. A natural application is the analysis of diffraction data measured during the AM build process or other extreme heating and cooling scenarios, such as quenching, to identify critical points of microstructural development and guide modeling of kinetics in constitutive models. However, even applying this analysis to understanding more traditional heat treatments for process modeling optimization could prove extremely valuable.

With the large number of non-linear dimensionality reduction techniques available, it is worth discussing choice of technique. In this work, the fact that the embedding aligned with our physical understanding of the deformation process (the state variable evolution) suggests that important physical information can be gleaned from a lower-dimensional manifold and justifies the use of dimensionality reduction generally. However, if we frame the goal as attempting to best preserve a path through microstructural space with a lower-dimensional representation, LLE is the most appropriate choice. Two major choices were made in the analysis: (1) whether to perform a global analysis of the data (full spectral analysis) or analyze the data in localized regions (local spectral analysis) and (2) which metric to use to best maintain data neighborhood structure. For choice (1), local support was deemed more appropriate as it was of most interest to analyze transients and as such, retention of the structure of the data from measurement to measurement was prioritized. Indeed, the sparse banded structure (Fig. 5) resulting from neighbors in a time series is consistent with our physical understanding of microstructural evolution. If manifold structure was not a concern, methods such as kernel principal component analysis [29] could be employed, while if locality was not key to the data structure, other manifold dimensionality techniques such as ISOMAP [30] would have been more appropriate. For choice (2), a preservation of the path-shape (angles) between measurements was chosen to be of most interest in order to capture deformation mechanism changes like the elastic-plastic transition. The immediate use of diffraction images provides for regular (and often close) sampling in time and detailed coverage of the selected (reciprocal) space with extremely low noise. As such, the demands of constructing the tangent may

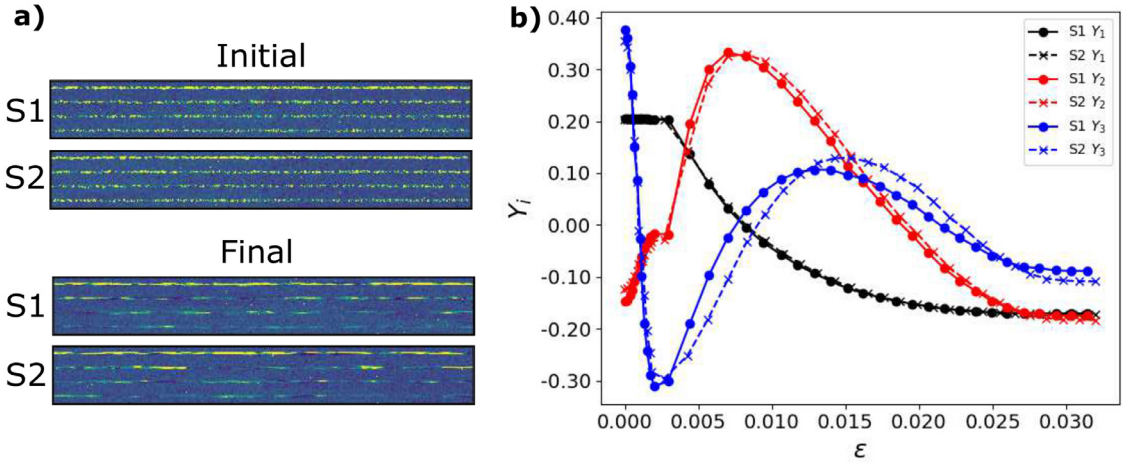

Fig. 8. (a) Comparison of initial and final measured diffraction peaks from sample 1 (S1) and sample 2 (S2). (b) The first three embedded coordinates recovered using LLE from the two samples plotted versus applied strain.

be avoided (Hessian LLE [1] and Local Tangent Space Alignment [31]) while capturing details of transients through use of relatively smaller neighborhoods. We note that the related Laplacian Eigenmap [32] technique may provide a possible alternative for the particular application considered herein if maintaining distance between measurements was deemed more critical. Looking beyond the present work, incremental LLE could be used on-the-fly during an *in-situ* X-ray experiment [33]. LLE provides a good match to the exercise under consideration, while offering general demonstration of insight garnered through lower-dimensional representations of high-dimensional measurements typical of X-ray science.

Beyond aiding the interpretation of observed mechanical response, the correlations between the embedded coordinates and the solutions to differential equations describing state variables (ρ_m and ρ_f) suggest a new paradigm for the development of constitutive models as the embeddings appear to be directly quantifying *the evolution of material state*. Rather than develop constitutive models to fit mechanical testing data such as macroscopic stress-strain responses, constitutive models can be developed that align with the discovered embedded coordinate data. Particularly for thermo-mechanical deformation model development, instead of using the embedding as a secondary validation of an established model (as in this work), evolution equations for microstructure could be developed that evolve in the same manner as the embeddings (i.e. having the same transient and saturation points). In addition, direct linking to state variables may not be necessary, forward modeling [5,34] of scattering could produce synthetic data that are processed in the same manner as experimental data and then directly compared. A major advance with this approach is that we will be building material models directly with microstructural data and the micromechanical response will now be a predicted by-product. Also, aligning models to LLE-determined embedded coordinates ensures comparison to microstructural descriptors that are orthogonal by construction.

As a test of the robustness of this approach to microstructural analysis, a second sample (S2) was deformed, probed, and analyzed in the same manner as the first (S1) to test if the same lower-dimensional representation would be recovered from different sets of grains and diffraction peaks. Fig. 8a shows the initial and final diffraction peaks from S1 and S2. In Fig. 8a, we can see distinct sets diffraction peaks from the illuminated grain ensembles that both smear out with applied load, but most importantly, different ensembles of grain orientations are being probed. Fig. 8b compares the first three embedded coordinates recovered from the diffraction peak time series from the two samples. The embedded coordinates recovered are very similar even though the collections of diffraction peak analyzed have significantly different structures. As would be expected from our interpretation of the embedded coordinates, the underlying behavior and rates of microstructure evolution between the two samples track well. The similarities between the two samples reinforce that LLE is discovering the same underlying, articulating deformation mechanisms, as would be expected from the same material.

We stress that in this correlation process, the state variables investigated are still posited by the researcher performing the analysis, but significantly more confidence can be placed in model results when there is strong correlation between state variable evolution and lower-dimensional representations of microstructure. Although guiding the development of physics-based material constitutive models with unsupervised learning data is a major alteration of current model development paradigms, the potential to accelerate model development is clear. Importantly, beyond deformation model development, the analysis method presented likely has wide applicability to other material characterization modalities and *in-situ* monitoring of process conditions, including technologically relevant processes such as additive manufacturing itself.

7. Conclusions

Locally linear embedding was used to reduced time series diffraction data collected during uniaxial tension of additively manufactured Inconel 625 down to a lower-dimensional representation of the microstructure (embedded coordinates). In this work we demonstrated that the embedded coordinates:

- capture the sharp microstructural transitions that occur during yield.
- appear to discover articulation points of the evolving state of the materials by showing strong correlations with modeled evolution of dislocation and defect populations in the material.
- are not directly tied to a single set of diffraction peaks from a material, but rather the underlying material state evolution.

Declaration of Competing Interest

The authors declare that they have no known competing financial interests or personal relationships that could have appeared to influence the work reported in this paper.

Acknowledgments

This work is based upon research conducted at the Center for High Energy X-ray Sciences (CHEXS) which is supported by the National Science Foundation under award DMR-1829070. AJB received support through the Office of Naval Research (Contract N00014-16-1-3126). The authors would like to thank Magnus Ahlfors at Quintus Technologies for performing the hot isostatic pressing treatment. The authors would like to thank Professor Matthew Miller, Dr. Kelly Nygren, Dr. Paul Shade, Dr. Nathan Barton, and Dr. Fan Zhang for helpful suggestions.

Supplementary material

Supplementary material associated with this article can be found, in the online version, at doi:10.1016/j.actamat.2019.10.011.

References

[1] D.L. Donoho, C. Grimes, Hessian eigenmaps: locally linear embedding techniques for high-dimensional data, Proc. Natl. Acad. Sci. 100 (10) (2003) 5591–5596, doi:10.1073/pnas.1031596100.
[2] L. Margulies, T. Lorentzen, H. Poulsen, T. Leffers, Strain tensor development in a single grain in the bulk of a polycrystal under loading, Acta Mater. 50 (7) (2002) 1771–1779.
[3] H. Poulsen, Three-Dimension X-Ray Diffraction Microscopy, 1st, Springer, 2004.
[4] P.P. Ewald, X-Ray diffraction by finite and imperfect crystal lattices, Proc. Phys. Soc. 52 (1) (1940) 167–174, doi:10.1088/0959-5309/52/1/323.
[5] R.M. Suter, D. Hennessy, C. Xiao, U. Lienert, Forward modeling method for microstructure reconstruction using x-ray diffraction microscopy: single-crystal verification, Rev. Sci. Instrum. 77 (12) (2006) 123905, doi:10.1063/1.2400017.
[6] S.F. Li, J. Lind, C.M. Hefferan, R. Pokharel, U. Lienert, A.D. Rollett, R.M. Suter, Three-dimensional plastic response in polycrystalline copper *via* near-field high-energy X-ray diffraction microscopy, J. Appl. Crystallogr. 45 (6) (2012) 1098–1108.
[7] M.A. Krivoglaz, X-ray and Neutron Diffraction in Nonideal Crystals, Springer Science & Business Media, 2012.
[8] L. Van Der Maaten, E. Postma, J. Van den Herik, Dimensionality reduction: a comparative review, J. Mach. Learn. Res. 10 (66–71) (2009) 13.
[9] S.T. Roweis, L.K. Saul, Nonlinear dimensionality reduction by locally linear embedding, Science 290 (5500) (2000) 2323–2326.
[10] E.A. Lass, M.R. Stoudt, M.E. Williams, M.B. Katz, L.E. Levine, T.Q. Phan, T.H. Gnaeupel-Herold, D.S. Ng, Formation of the ni3nb δ-phase in stress-relieved inconel 625 produced via laser powder-bed fusion additive manufacturing, Metall. Mater. Trans. A 48 (11) (2017) 5547–5558, doi:10.1007/s11661-017-4304-6.
[11] , ASTM F3056-14e1, Standard Specification for Additive Manufacturing Nickel Alloy (UNS N06625) with Powder Bed Fusion, Technical Report, ASTM International, West Conshohocken, PA, 2014.
[12] F. Bachmann, R. Hielscher, H. Schaeben, Texture analysis with mtex–free and open source software toolbox, Solid State Phenom. 160 (2010) 63–68.
[13] ISO / ASTM52921 - 13, Standard Terminology for Additive Manufacturing-Coordinate Systems and Test Methodologies, Technical Report, ASTM International, West Conshohocken, PA, 2013.
[14] P.A. Shade, B. Blank, J.C. Schuren, T.J. Turner, P. Kenesei, K. Goetze, R.M. Suter, J.V. Bernier, S.F. Li, J. Lind, U. Lienert, J. Almer, A rotational and axial motion system load frame insert for in situ high energy x-ray studies, Rev. Sci. Instrum. 86 (9) (2015) 093902, doi:10.1063/1.4927855.
[15] L.K. Saul, S.T. Roweis, Think globally, fit locally: unsupervised learning of low dimensional manifolds, J. Mach. Learn. Res. 4 (Jun) (2003) 119–155.
[16] F. Pedregosa, G. Varoquaux, A. Gramfort, V. Michel, B. Thirion, O. Grisel, M. Blondel, P. Prettenhofer, R. Weiss, V. Dubourg, J. Vanderplas, A. Passos, D. Cournapeau, M. Brucher, M. Perrot, E. Duchesnay, Scikit-learn: machine learning in Python, J. Mach. Learn. Res. 12 (2011) 2825–2830.
[17] Y. Estrin, L. Kubin, Local strain hardening and nonuniformity of plastic deformation, Acta Metall. 34 (12) (1986) 2455–2464, doi:10.1016/0001-6160(86)90148-3.
[18] U. Kocks, Laws for work-hardening and low-temperature creep, J. Eng. Mater. Technol. 98 (1) (1976) 76–85.
[19] H. Mecking, U. Kocks, Kinetics of flow and strain-hardening, Acta Metall. 29 (11) (1981) 1865–1875, doi:10.1016/0001-6160(81)90112-7.
[20] C.U. Brown, G. Jacob, M. Stoudt, S. Moylan, J. Slotwinski, A. Donmez, Interlaboratory study for nickel alloy 625 made by laser powder bed fusion to quantify mechanical property variability, J. Mater. Eng. Perform. 25 (8) (2016) 3390–3397.
[21] P. Rodríguez, B. Wohlberg, Efficient minimization method for a generalized total variation functional, IEEE Trans. Imag. Proc. 18 (2) (2009) 322–332.
[22] R. Chartrand, B. Wohlberg, Total-variation regularization with bound constraints, in: Proceedings of the IEEE International Conference on Acoustics, Speech and Signal Processing, IEEE, 2010, pp. 766–769.
[23] J. Flinn, D. Field, G. Korth, T. Lillo, J. Macheret, The flow stress behavior of ofhc polycrystalline copper, Acta Mater. 49 (11) (2001) 2065–2074, doi:10.1016/S1359-6454(01)00102-1.
[24] K.J.H. Al-Fadhalah, C.-M. Li, A. Beaudoin, D. Korzekwa, I. Robertson, Microplastic processes developed in pure ag with mesoscale annealing twins, Acta Mater. 56 (19) (2008) 5764–5774, doi:10.1016/j.actamat.2008.07.050.
[25] P.S. Follansbee, Analysis of deformation in inconel 718 when the stress anomaly and dynamic strain aging coexist, Metall. Mater. Trans. A 47 (9) (2016) 4455–4466.
[26] A.M. Beese, Z. Wang, A.D. Stoica, D. Ma, Absence of dynamic strain aging in an additively manufactured nickel-base superalloy, Nat. Commun. 9 (1) (2018) 2083.
[27] C. Fressengeas, A. Beaudoin, M. Lebyodkin, L. Kubin, Y. Estrin, Dynamic strain aging: a coupled dislocation-solute dynamic model, Mater. Sci. Eng. A 400–401 (2005) 226–230 Dislocations 2004, doi:10.1016/j.msea.2005.02.073.
[28] K. Chatterjee, J. Ko, J. Weiss, H. Philipp, J. Becker, P. Purohit, S. Gruner, A. Beaudoin, Study of residual stresses in Ti-7Al using theory and experiments, J. Mech. Phys. Solids 109 (2017) 95–116, doi:10.1016/j.jmps.2017.08.008.
[29] B. Schölkopf, A. Smola, K.-R. Müller, Nonlinear component analysis as a kernel eigenvalue problem, Neural Comput. 10 (5) (1998) 1299–1319.
[30] J.B. Tenenbaum, V. De Silva, J.C. Langford, A global geometric framework for nonlinear dimensionality reduction, Science 290 (5500) (2000) 2319–2323.
[31] Z. Zhang, H. Zha, Principal manifolds and nonlinear dimensionality reduction via tangent space alignment, SIAM J. Sci. Comput. 26 (1) (2004) 313–338.
[32] M. Belkin, P. Niyogi, Laplacian eigenmaps and spectral techniques for embedding and clustering, in: Advances in Neural Information Processing Systems, 2002, pp. 585–591.
[33] O. Kouropteva, O. Okun, M. Pietikäinen, Incremental locally linear embedding, Pattern Recognit. 38 (10) (2005) 1764–1767, doi:10.1016/j.patcog.2005.04.006.
[34] D. Pagan, M. Miller, Connecting heterogeneous single slip to diffraction peak evolution in high-energy monochromatic X-ray experiments, J. Appl. Crystallogr. 47 (3) (2014) 887–898.